This is the post peer-review accepted manuscript of:

E. Idà, D. Marian and M. Carricato, "A Deployable Cable-Driven Parallel Robot With Large Rotational Capabilities for Laser-Scanning Applications," in IEEE Robotics and Automation Letters, Vol. 5 , Issue: 3, pp. 4140 – 4147, July 2020.

doi: 10.1109/LRA.2020.2989669

The published version is available online at:

https://ieeexplore.ieee.org/document/9076279

© 2020 IEEE. Personal use of this material is permitted. Permission from IEEE must be obtained for all other uses, in any current or future media, including reprinting/republishing this material for advertising or promotional purposes, creating new collective works, for resale or redistribution to servers or lists, or reuse of any copyrighted component of this work in other works.

A Deployable Cable-Driven Parallel Robot with Large Rotational Capabilities for Laser-Scanning Applications

Edoardo Idà[1], *IEEE Member*, Daniele Marian[2] and Marco Carricato[1], *IEEE Senior Member*

***Abstract*—This paper presents a novel Cable-Driven Parallel Robot dedicated to laser-scanning operations. The proposed device can inspect low-accessibility environments thanks to a self-deployable end-effector, which can be inserted in a closed container through very small access areas, such as hatches, pipes, etc. The reconfigurable end-effector is suspended and actuated by extendable cables, and is equipped with an optical mirror, which is used to deflect a laser beam produced by a frame-fixed laser distance sensor. Thanks to its large orientation capabilities, the machine can record the position of points belonging to a large portion of the surface to be scanned, primarily by tilting and panning the end-effector. The robot is equipped with a frame-orientation calibration device, which can align the machine frame to earth gravity before operation. The robot capabilities are validated by a prototype, which experimentally reconstruct benchmark surfaces.**

***Index Terms*—Field Robots, Industrial Robots, Parallel Robots**

I. INTRODUCTION

LASER scanner systems are fairly mature devices and are widely available on the market. They can be used to digitally reconstruct 3D environments by recording the distances of pointed objects with respect to the laser itself. They can be operated by people on the ground [1], on aircrafts [2] or can autonomously run on automatic machinery or robots [3]. Depending on the goal of 3D reconstruction, they may be characterized by high accuracy, which is preferable in order to detect micro-details on small objects, or they may be employed in wide-range measurements, where the system repeatability is instead of primary importance. Their use can be relatively simple in a wide and open environment, whereas difficulties may arise if the volume to be inspected is closed, not freely accessible or even dangerous. For example, the inner volume (typically around $250\ \mathrm{m}^3$) of fuel storage tanks (Fig. 1) is filled with explosive gases and liquid fuel, and it has to be periodically measured without emptying its content. This measurement is performed by calculating the volume enclosed by a digital reconstruction of the tank inner surface, which can be accessed either by removing some portions of the tank [4], which is undesirable in practice, or by introducing suitable mechanical devices through narrow inspection hatches (roughly $5\,\mathrm{cm}$ wide) [5]. The latter alternative has some drawbacks in terms of transportability and ease of use; in fact, the long lead screw ordinarily employed to move the laser optical mirror inside the tank limits inspection capabilities and leads to an unwieldy machine.

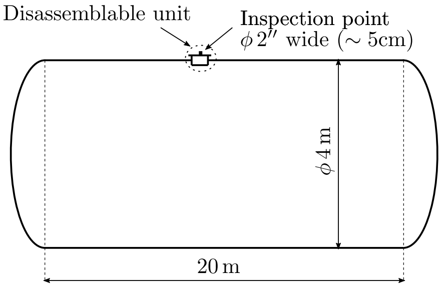

Figure 1: Schematics of a typical fuel storage tank

A multi degree-of-freedom (*DoF*) robotic solution, which is able to meet the application requirements in terms of size, precision and ease of use, may prove to be a valid alternative to the aforementioned devices, which are the application standard so far. Cable-driven parallel robots (*CDPRs*) are a class of robotic manipulators where the end-effector (*EE*) is displaced by means of servo-actuated extendable cables. Their use has been proposed in several applications, ranging from logistics [6] to haptics [7]. *CDPRs* appear to be adequate for non-contact processes [8], [9], such as the deflection of a distance-measuring laser beam on a platform-mounted mirror, and their mechanical structure is effective in reducing machine size and enhancing deployability [10], [11]. Their translational workspace can be easily scaled from some cubic centimeters [7] to hundreds of cubic meters [9], thus representing a robotic solution that can be adapted to the application at hand. On the other hand, common *CDPR* designs usually ensure a large translational workspace, while the orientation capability of the *EE* is limited by the necessity to avoid cable collisions [12], or to prevent cables from becoming slack [13]. New *CDPR* designs that allow for a larger orientation workspace are emerging in recent years, with their key features being articulated end-effectors [14]–[16], reconfigurable bases [17] or additional constraining mechanisms [18].

In this paper, we propose a novel 6-cable 6-*DoF* suspended

Manuscript received: December, 19, 2020; Revised February, 6, 2020; Accepted April, 15, 2020.

This paper was recommended for publication by Editor Dezhen Song upon evaluation of the Associate Editor and Reviewers' comments.

This work was financially supported by Green Line S.r.l., Via Circonvallazione Nuova, 27 - 47923 Rimini (RN), Italy

[1] Edoardo Idà and Marco Carricato are with the Dept. of Industrial Engineering, University of Bologna, 40137 Bologna, Italy, {edoardo.ida2,marco.carricato}@unibo.it

[2] Daniele Marian is with Te.S.I. S.r.l, 48123, Ravenna, Italy, daniele.marian@tesiengineering.com

and deployable *CDPR* for laser-scanning-based inspections, which consists of:

- an industrial linear-distance laser measurement device fixed to the robot frame;
- a deployable *EE*, which can be inserted through a narrow access area, can be automatically deployed after insertion, and exhibits a wide orientation workspace;
- cable actuation units, which displace and orient the *EE*;
- an optical mirror mounted on the *EE*, which deflects the laser beam;
- a 2-*DoF* frame-orientation calibration device consisting of an industrial inclinometer and two extendable motorized support legs.

Because of the suspended nature of the manipulator, its orientation workspace is dependent on the direction and magnitude of the external wrenches (such as gravity) applied to the *EE*. The frame-orientation device automatically aligns the machine laser beam, and thus its frame, with the earth gravity before any robot operation: this fact results in a predictable and repeatable robot workspace, independent of the deployment site. The proposed robot is validated by a full-scale prototype, which is used to reconstruct the shape of benchmark surfaces: amply redundant measurements are employed for a linear least-square data fitting of the mathematical model of the surfaces.

The structure of the paper is as follows. Section II introduces the robot kinematics and the laser system. The machine design is described in Section III. Section IV studies the manipulator statics and its wide orientation workspace. Finally, Section V demonstrates the robot capabilities by the experimental reconstruction of known planar surfaces.

II. KINEMATIC MODEL

We consider a fully-actuated *CDPR* consisting of a mobile platform coupled to the base by 6 cables, which are coiled and uncoiled by motorized winches. $Oxyz$ is an inertial frame, whereas $Px'y'z'$ is a mobile frame attached to the moving platform so that the coordinate plane $Px'y'$ coincides with the top surface of the mirror. $\mathbf{i}$, $\mathbf{j}$, $\mathbf{k}$ (resp. $\mathbf{i}'$, $\mathbf{j}'$, $\mathbf{k}'$) are unit vectors along the coordinate axes of $Oxyz$ (resp. $Px'y'z'$). The platform pose in $Oxyz$ is described by the position vector $\mathbf{p}$ of P, and the rotation matrix $\mathbf{R}$. The laser beam is emitted from the origin O and it is aligned with the z axis. $\mathbf{R}$ is conveniently parametrized by tilt-and-torsion (*TT*) angles $\boldsymbol{\epsilon} = [\phi, \theta, \psi]^T$ [19]:

$$\mathbf{R}(\phi,\theta,\psi) = \mathbf{R}_a(\phi,\theta)\mathbf{R}_z(\psi) \tag{1}$$

$$\mathbf{R}_a(\phi,\theta) = \mathbf{R}_z(\phi)\mathbf{R}_y(\theta)\mathbf{R}_z(-\phi) \tag{2}$$

where a is a line obtained by rotating the y-axis by ϕ around the z-axis, $\mathbf{R}_a(\phi,\theta)$ is a rotation θ about a, $\mathbf{R}_y(\cdot)$ and $\mathbf{R}_z(\cdot)$ are elementary rotation matrices about the y and z axes.

Cables are modelled as inextensible straight line segments. Each cable is guided from the winch into the workspace through an eyelet at point B_i, identified by position vector $\mathbf{b}_i$ in $Oxyz$, and attached to the platform at point A_i (Fig. 2). The coordinates of A_i and of the platform center of mass Q are described in the mobile frame by $\mathbf{a}_i'$ and $\mathbf{q}'$, respectively, and in the inertial frame by:

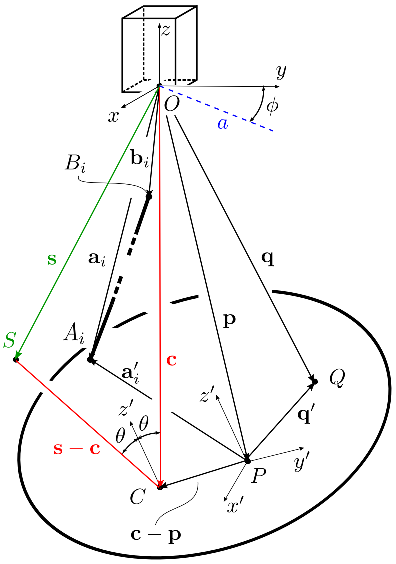

Figure 2: Geometry of the cable-driven laser-scanner

$$\mathbf{a}_i = \mathbf{p} + \mathbf{R}\mathbf{a}_i', \qquad \mathbf{q} = \mathbf{p} + \mathbf{R}\mathbf{q}' \tag{3}$$

The constraints imposed by the cables on the platform are:

$$\|\boldsymbol{\rho}_i\|^2 - l_i^2 = \|\mathbf{a}_i - \mathbf{b}_i\|^2 - l_i^2 = 0, \qquad i = 1, \cdots, 6 \tag{4}$$

where $\boldsymbol{\rho}_i$ is the vector from B_i to A_i, and l_i is the i-th cable length. For control purpose, Eq. (4) can be solved for l_i, once $\mathbf{p}$ and $\mathbf{R}$ are assigned.

The laser kinematic model is needed in order to determine the coordinates of a measured point S is the inertial frame, once $\mathbf{p}$, $\mathbf{R}$ and the laser measurement d are known. The laser beam is composed of two line segments, whose total length is d. The former line segment is aligned with the z axis and intersects the mirror in point C at height z_C, so that the position vector of C in $Oxyz$ is $\mathbf{c} = z_C\mathbf{k}$. The latter line segment is reflected on the mirror with an angle of reflection equals to the angle of incidence θ and meets the measured surface in S.

Since both P and C belong to the $x'y'$ plane:

$$(\mathbf{c} - \mathbf{p}) \cdot \mathbf{k}' = 0 \quad \Longrightarrow \quad z_C = \big(\mathbf{p} \cdot \mathbf{k}'\big)/(\mathbf{k} \cdot \mathbf{k}') \tag{5}$$

where:

$$\mathbf{k}' = \mathbf{R}\mathbf{k} = \mathbf{R}_a(\phi,\theta)\mathbf{k} \tag{6}$$

The position of point S can be determined as:

$$\begin{aligned}\mathbf{s} = z_C\mathbf{k} + (d - z_C)\mathbf{R}_a(\phi, 2\theta)\mathbf{k} &= \\ = \big[z_C\mathbf{I}_{3\times3} + (d - z_C)\mathbf{R}_a(\phi, 2\theta)\big]\mathbf{k}\end{aligned} \tag{7}$$

where $\mathbf{I}_{3\times3}$ is the 3×3 identity matrix.

III. *CDPR* DESIGN

The need to easily transport and deploy the robot requires a compact and lightweight design. In addition, the scanning process must be carried out by accessing the operative

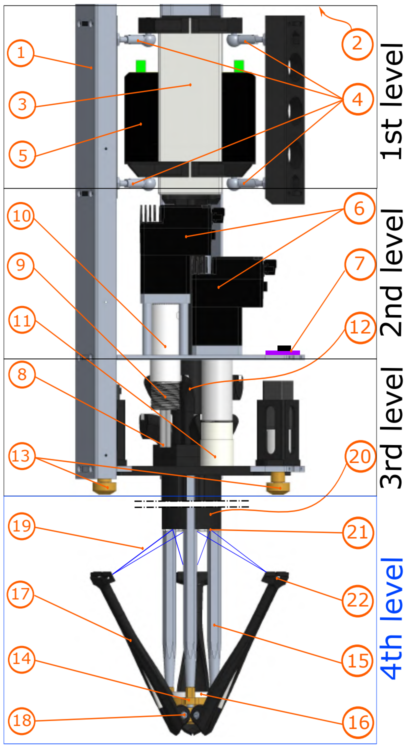

Figure 3: Cad model of the cable-driven laser-scanner

environment through a small opening. Lastly, the presence of explosive gases in one of the machine possible target applications inhibits the use of any electrical equipment inside the volume to be inspected: sensors, actuators, control boards, etc. should be decentralized. These requirements suggests the use of a suspended, completely actuated, 6-*DoF EE*, to be inserted and remotely commanded from an elevated position. The use of additional cables for a redundant actuation would provide a larger wrench-feasible workspace, but also (i) increase machine cost, size and weight and (ii) introduce additional model uncertainties [20] which could deteriorate machine performance, if not accounted for. Figure 3 shows a CAD model of the cable-driven laser scanner, where some repeated components have been hidden for clarity sake. The machine frame (1) is composed of parallel aluminum plates, linked by three steel sheets, which divide the machine volume in several levels. Electromagnetic pulse sensible electronic components, such as control boards (2 - STM32 NUCLEO-H743ZI) and communication peripherals, are located in the upper part of the machine and are not displayed in Fig. 3. The first level is equipped with the laser sensor (3 - Dimetix AG DLS-C 15) and its position-and-orientation regulation unit (4); 2 DC power regeneration units (5 - Moons RC880) are mounted on the same plate supporting the laser.

On the second level, 6 ServoStep motors (6 - Moons TSM17P 3AG) are positioned in an axial-symmetric fashion. These actuators feature high torque density and servo-control capabilities, which makes them ideal for compact, limited-speed and direct-drive winches. An inclinometer board (7 - Murata SCA100T D02), mounted next to the motors, provides the system with gravity-alignment feedback.

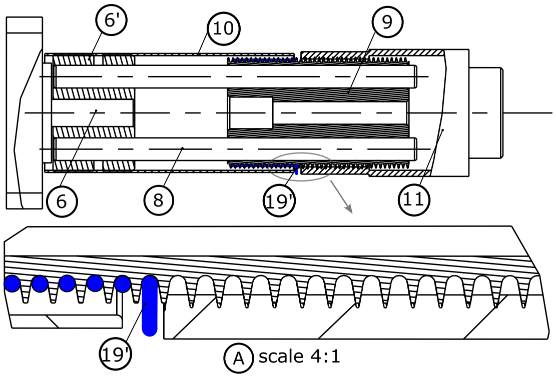

Figure 4: Cross-section of a winch with detailed view (A) of the cable fixed exit point and of the helical joint between the drum and the cap

On the third level, robot winches comprise rototranslating drums [21] (see Fig. 4 for a cross-section view): two rods (8) are rigidly linked to each motor shaft with a custom rigid coupling (6’). The rods transmit rotational motion to an externally-threaded drum (9), which is free to translate with respect to them. The cable is coiled and uncoiled onto the thread groove and a drum cover (10) protects it from accidental derailment; lastly, an internally threaded cap (11) ensures the overall helicoidal motion of the drum, so that the cable exit point from its groove (19’) is fixed. Cables are then conveyed into a central column (12), which routes them from the 3rd level (which is outside the inspected volume) to the 4th level (which is inside the inspected volume).

Beside the winches, one fixed and two actuated pins (13) are the contact points of the machine with a support surface, such as a pipe flange. Thanks to the inclinometer feedback, the pins are elongated/retracted so as to align the z-axis with the earth gravity direction before any robot operation. On the 4th level, the self-deployable *EE* is composed of a main brass body (14), which is referenced in its home configuration to the frame (15) by 3 spikes, an optical-grade mirror (16 - Edmund Optics $\lambda/20$ enhanced aluminium mirror) and 3 petals (17), which can rotate with respect to the main body about radial bearings (18). In order to minimize frictional effects, cables (19 - Daiwa Saltiga 12 braids, $0.55\mathrm{mm}$ diameter) have a special silicon cover that ensures high roundness of their cross-section and low friction coefficient. They exit the teflon-covered routing tube (20) from proximal eyelets (21) and are attached in pairs inside a distal eyelet (22) onto each petal.The weight ratio between the platform components (14,16,17,18) and the total amount of cable installed in the machine ($12\ \mathrm{m}$) is greater than 10^2, thus allowing cable to be assumed massless. When the main body is constrained by the frame, the petals can be closed by coiling the cables: this operation is performed when homing the machine before scanning (see the attached media). When the platform has to be deployed, cables are uncoiled and axial springs, embedded in each petal, provide the torque necessary to rotate the latters towards a mechanical stop. After petal motion is completed, the platform disengages its referencing spikes and becomes effectively suspended by its 6 cables.

Table I: *CDPR* geometric properties

[mm]	$\mathbf{b}_1$	$\mathbf{b}_2$	$\mathbf{b}_3$	$\mathbf{b}_4$	$\mathbf{b}_5$	$\mathbf{b}_6$	$\mathbf{a}'_1$	$\mathbf{a}'_2$	$\mathbf{a}'_3$	$\mathbf{a}'_4$	$\mathbf{a}'_5$	$\mathbf{a}'_6$
x	-1	1	10.9	9.9	-9.9	-10.9	-130	130	130	0	0	-130
y	12	12	-5.1	-6.9	-6.9	-5.1	75	75	75	-150	-150	75
z	0	0	0	0	0	0	-5	-5	-5	-5	-5	-5

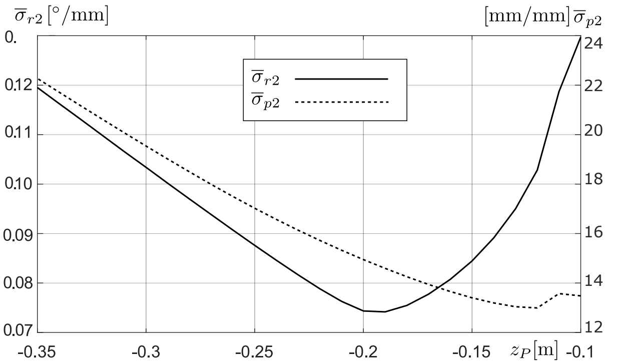

Figure 5: Global sensitivity indexes

The *CDPR* design was primarily driven by application requirements, with the ultimate goal to achieve autonomous deployability, a wide-orientation workspace, and a reasonable *EE* stiffness. Since the *CDPR* base and *EE* must be able to access the operative space through a narrow 5cm-wide opening, the undeployed robot must lie within a 4.5cm-diameter cylinder, with proximal eyelets being located on a 2.5cm-diameter circle. The distal eyelets are located at the end of deployable petals: the more numerous the petals, the smaller their breadth and, thus, their bending stiffness after deployment. This suggests to use only 3 equally-spaced petals and to locate distal eyelets at their extremities in pairs. The resulting architecture, with eyelets located in pairs at the vertices of equilateral triangles on both the base and the *EE*, also follows the optimization of the orientation capability index discussed in Section IV, thus guaranteeing the largest orientation workspace (similarly to [22]). According to this criterion, the distal eyelets should be kept as far as possible from the *EE* reference point, but this also increases the petals' length and bending compliance. The final *EE* geometry (a triangle inscribed in a 30cm-diameter circle) is a compromise that allows, in condition of maximum load, an end deflection of the petals not higher than 0.05mm.

IV. STATIC MODEL AND ORIENTATION WORKSPACE

The orientation workspace of the cable-driven platform is characterized by the set of *TT* angles that can be attained while reference point P is fixed [19] and cable tension magnitudes lie within two positive scalars $\underline{\tau}$ and $\overline{\tau}$, with $0 \leq \underline{\tau} \leq \overline{\tau}$ [13]. In a given pose, the array $\boldsymbol{\tau}$ of cable tensions is evaluated by the static model of the robot:

$$-\mathbf{K}^T\boldsymbol{\tau} + \mathbf{w}_e = 0 \tag{8}$$

$$\mathbf{K} = \begin{bmatrix} \hat{\boldsymbol{\rho}}_1^T & -\hat{\boldsymbol{\rho}}_1^T\mathbf{R}\tilde{\mathbf{a}}'_1\mathbf{R}^T \\ \vdots & \vdots \\ \hat{\boldsymbol{\rho}}_6^T & -\hat{\boldsymbol{\rho}}_6^T\mathbf{R}\tilde{\mathbf{a}}'_6\mathbf{R}^T \end{bmatrix}, \qquad \mathbf{w}_e = m\begin{bmatrix} \mathbf{g} \\ \mathbf{R}\tilde{\mathbf{q}}'\mathbf{R}^T\mathbf{g} \end{bmatrix} \tag{9}$$

where $\mathbf{K}$ is the inverse Jacobian matrix of the manipulator, m is the *EE* mass, $\mathbf{g} = -9.81\,\mathbf{k}$ is the gravitational acceleration, $\mathbf{w}_e$ is the external (gravitational) load acting on the platform, $(\hat{\cdot})$ and $(\tilde{\cdot})$ respectively denote the direction and the skew-symmetric representation of a vector.

Since the orientation workspace depends on the *EE* position, it is of interest to evaluate it for several values of $\mathbf{p}$. The quality of the performance of the robot for a given position can be used as a comparison between different orientation workspaces. The global condition index [23] is commonly employed, but it suffers from the fact that Jacobian matrices are not dimensionally consistent. Thus, in order to infer the *manipulator rotation and P-displacement sensitivity to actuator displacements*, we will consider the maximum-magnitude rotation σ_{r2} and point-displacement σ_{p2}, under a unit 2-norm actuator error [24]. If we define $\mathbf{K}_p, \mathbf{K}_r \in \mathbb{R}^{6\times 3}$ so that $\mathbf{K} = [\mathbf{K}_p \; \mathbf{K}_r]$, and consider small actuation error $\delta\mathbf{l}$, platform displacement $\delta\mathbf{p}$ and rotation $\delta\mathbf{r}$, such that $\delta\mathbf{l} = \mathbf{K}_p\delta\mathbf{p} + \mathbf{K}_r\delta\mathbf{r}$, σ_{r2} and σ_{p2} are:

$$\sigma_{r2} = \max_{\|\delta\mathbf{l}\|_2=1} \|\delta\mathbf{r}\|_2 = \sqrt{\|\left(\mathbf{K}_r^T\mathbf{P}_p\mathbf{K}_r\right)^{-1}\|_2} \tag{10}$$

$$\sigma_{p2} = \max_{\|\delta\mathbf{l}\|_2=1} \|\delta\mathbf{p}\|_2 = \sqrt{\|\left(\mathbf{K}_p^T\mathbf{P}_r\mathbf{K}_p\right)^{-1}\|_2} \tag{11}$$

where $\mathbf{P}_p, \mathbf{P}_r \in \mathbb{R}^{6\times 6}$ are defined as:

$$\mathbf{P}_p = \mathbf{I}_{6\times 6} - \mathbf{K}_p\left(\mathbf{K}_p^T\mathbf{K}_p\right)^{-1}\mathbf{K}_p^T \tag{12}$$

$$\mathbf{P}_r = \mathbf{I}_{6\times 6} - \mathbf{K}_r\left(\mathbf{K}_r^T\mathbf{K}_r\right)^{-1}\mathbf{K}_r^T \tag{13}$$

These indexes assume the actuators' errors to be dependent, which is physically unrealistic, as opposed to sensitivity indexes $\sigma_{r\infty}$ and $\sigma_{p\infty}$, based on the infinity-norm of $\delta\mathbf{l}$, which would offer a sound physical interpretation [24], [25]. However, σ_{r2} and σ_{p2} can be computed in closed form, which is a useful property for a rapid performance evaluation. and they reasonably approximate $\sigma_{r\infty}$ and $\sigma_{p\infty}$. σ_{r2} and σ_{p2} provide information about the local performance of a manipulator, but global counterparts can be defined as:

$$\overline{\sigma}_{r2} = \frac{\sum_{i=1}^{\kappa}\sigma_{r2,i}}{\kappa}, \qquad \overline{\sigma}_{p2} = \frac{\sum_{i=1}^{\kappa}\sigma_{p2,i}}{\kappa} \tag{14}$$

and used to compare orientation workspaces computed over κ sampling configurations. As an example, the global sensitivity indexes for $\mathbf{p} = [0, 0, z_P]^T\text{m}$, with $-0.35 \leq z_P \leq -0.1\text{m}$ are portrayed in Fig. 5. Indexes are not monotonic over z_p, but have minima: thus, for a given robot design, there are

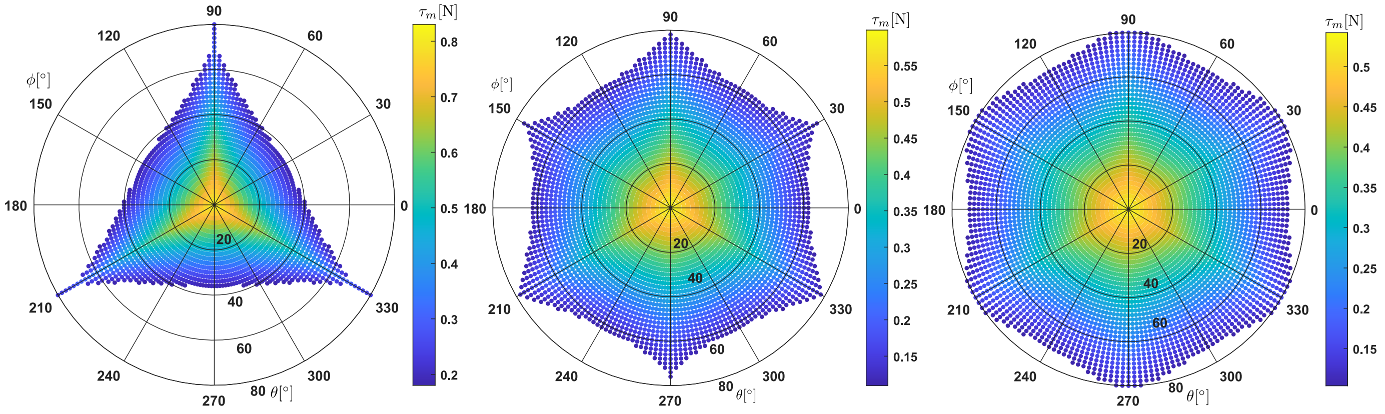

(a) τ_m, $\mathbf{p} = [0, 0, -0.1]^T\,\mathrm{m}$ (b) τ_m, $\mathbf{p} = [0, 0, -0.2]^T\,\mathrm{m}$ (c) τ_m, $\mathbf{p} = [0, 0, -0.3]^T\,\mathrm{m}$

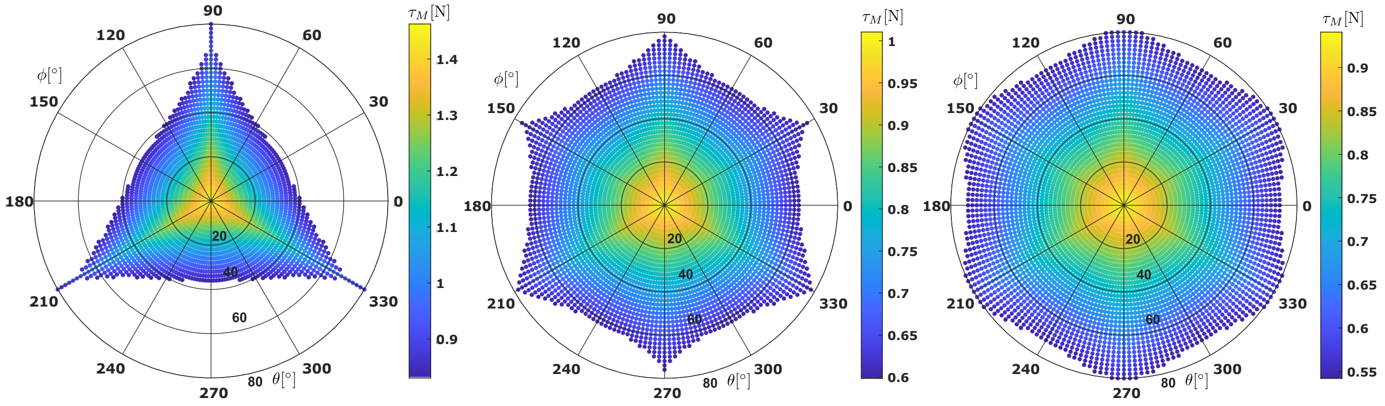

(d) τ_M, $\mathbf{p} = [0, 0, -0.1]^T\,\mathrm{m}$ (e) τ_M, $\mathbf{p} = [0, 0, -0.2]^T\,\mathrm{m}$ (f) τ_M, $\mathbf{p} = [0, 0, -0.3]^T\,\mathrm{m}$

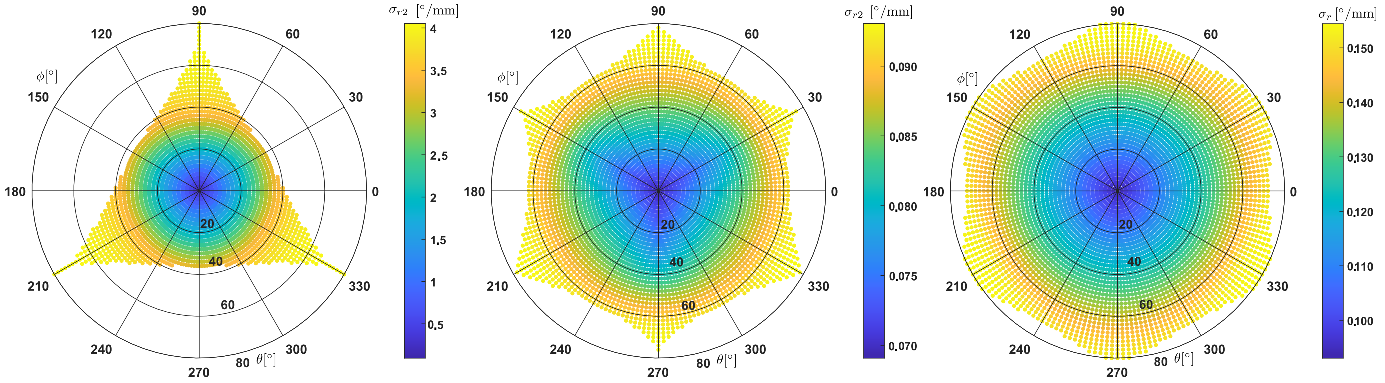

(g) σ_{r2}, $\mathbf{p} = [0, 0, -0.1]^T\,\mathrm{m}$ (h) σ_{r2}, $\mathbf{p} = [0, 0, -0.2]^T\,\mathrm{m}$ (i) σ_{r2}, $\mathbf{p} = [0, 0, -0.3]^T\,\mathrm{m}$

Figure 6: Zero torsion orientation workspace highlighting τ_m, τ_M and σ_{r2} for decreasing values of z_P

vertical heights where the robot will be in general more accurate in terms of its *EE* orientation (minimum of σ_{r2}) or displacement (minimum of σ_{p2}); on the other hand, the corresponding orientation workspace may not be large enough for the given task, so that a neighboring position could be selected as a trade-off between point-displacement and orientation accuracy, and orientation capabilities, depending on application requirements. Zero-torsion orientation workspaces for $z_p = -0.1$, -0.2, $-0.3\mathrm{m}$ are portrayed in Fig. 6 in polar coordinates, where ϕ and θ are plotted in the circumferential and in the radial direction, respectively. In Figs. 6a, 6b, 6c, each workspace sampling point is assigned a color according to the value of minimum cable tension τ_m, determined by solving Eq. (8) for τ; in Figures 6d, 6e, 6f and 6g, 6h, 6i the color represents, respectively, the maximum cable tension τ_M and rotation sensitivity σ_{r2}. The geometric properties of the *CDPR* under consideration are reported in Tab. I, *EE* mass is $m = 0.3\,\mathrm{Kg}$, and cable tension limits are set equally for each cable as $\underline{\tau} = 0.1\,\mathrm{N}$ and $\overline{\tau} = 10\,\mathrm{N}$. Zero-torsion is imposed mainly for two reasons:

- it is easier to visualize the workspace in polar coordinates on a 2D plot;
- the manipulator task, that is, the deflection of the laser beam for the detection of point S, is not dependent on

the platform torsion according to Eq. (7).

The analysis of Fig. 6 highlights several aspects of the proposed *CDPR* architecture:

- workspace limits are always reached for an increasing value of θ because one of the cable reach the lower tension limit $\underline{\tau}$ and never the superior limit $\overline{\tau}$; the latter, however, can be reached in case $z_P \rightarrow 0$ (which is mechanically non possible, in our case);
- the ratio $\max(\boldsymbol{\tau})/\min(\boldsymbol{\tau})$, for an assigned orientation, is decreasing with z_P, and in any case has an upper bound: this fact expedites mechanical design and control algorithms development, possibly helping in the inclusion of additional linear elasticity effects;
- orientation workspace is large, compared to both standard *CDPR* architectures and rigid-link parallel robots.

V. EXPERIMENTAL RESULTS

A prototype of the proposed robot was realized and used to reconstruct planar benchmark surfaces in laboratory conditions (see Fig. 7): three vertical planar surfaces were laid around the robot and the surrounding volume was covered, so that any strong light source could limitedly affect experiment results. The machine was placed on a three-legged table with a central hole of $5\,\mathrm{cm}$ diameter. After the robot is switched on, the gravity alignment procedure aligns $\mathbf{k}$ with $\mathbf{g}$. Then, the homing procedure is performed (Fig. 8a), with cables being coiled until the servostep motors reach a stall condition, which is caused by the robot frame impeding further petal motion: homing operation requires fine tuning because of the overactuation of the petal (two cables are pulling a 1-*DoF* rigid body) during this phase. For demonstration purpose, it was chosen to reconstruct the benchmark surfaces by first automatically deploying the platform (Fig. 8b), then displacing it to $\mathbf{p} = [0, 0, -0.2]^T \mathrm{m}$ (Fig. 8c), and finally by performing a series of successive rotational displacements with $\phi \in [0, 360)^\circ$, $\theta \in [10, 60]^\circ$ and $\psi = 0^\circ$ (Fig. 8d for maximum tilting). These operating conditions were chosen according to Fig. 6 results, as a trade-off between robot accuracy and orientation workspace size.

Control set-points, which are *EE* poses, are transformed into cable-length set-points according to Eq. (4), and fed to the servo-step motors. Points on the planar surfaces were reconstructed according to Eq. (7). Then, the results were exported and, after filtering out outliers (such as the table legs), they were clustered in 3 groups of i points ($j = 1, 2, 3$, $i = 1, \ldots, \lambda_j$). If we consider the equation of a plane not passing through the origin O:

$$\mathbf{s}_i^j \cdot \mathbf{n}^j + 1 = 0; \tag{15}$$

where $\mathbf{s}_i^j$ is any point i of cluster j and $\mathbf{n}^j$ is the unit vector normal to the j-th plane divided by the plane distance from the origin, the reconstruction of planar surfaces can be conducted according to a least-square identification [26] model:

$$\mathbf{A}^j \mathbf{n}^j = \mathbf{1}_{\lambda_j} \tag{16}$$

where:

$$\mathbf{A}^j = \begin{bmatrix} \mathbf{s}_1^j & \cdots & \mathbf{s}_{\lambda_j}^j \end{bmatrix}^T, \; \mathbf{1}_{\lambda_j} = \begin{bmatrix} 1 & \cdots & 1 \end{bmatrix}^T \tag{17}$$

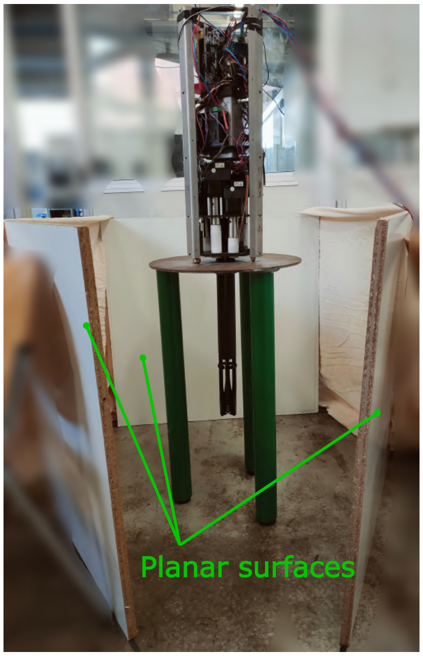

Figure 7: Robot prototype and experimental conditions

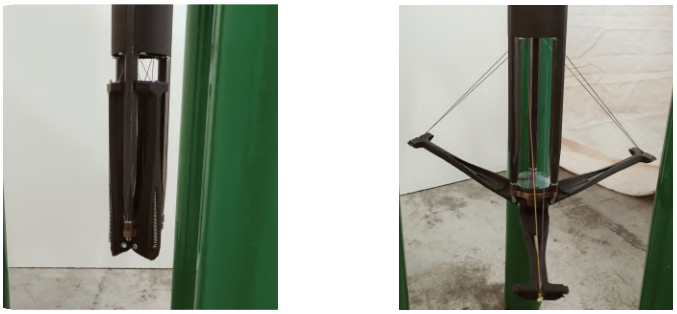

(a) Closed *EE*

(b) Deployed *EE*

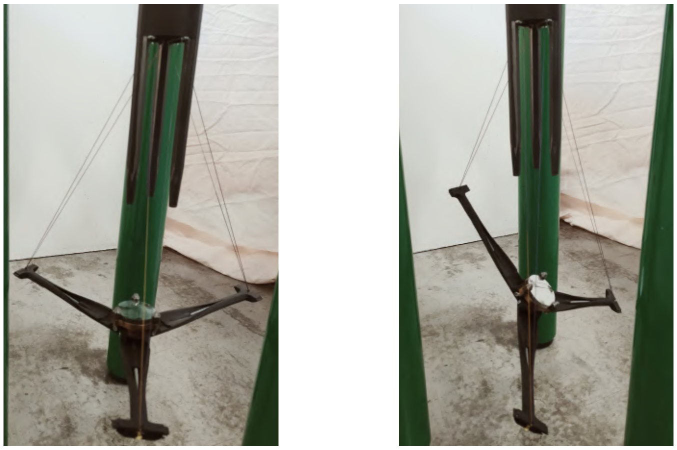

(c) *EE* at $\mathbf{p} = [0, 0, -0.2]^T \mathrm{m}$

(d) *EE* at $\mathbf{p}$, $\boldsymbol{\epsilon} = [0, 60, 0]^{T\circ}$

Figure 8: Experiment conditions

Table II: Experiments results

	Test 1	Test 2	Test 3
$\overline{\mathbf{n}}^1$	$[-1.9574; -0.8582; 0.1225]^T$	$[-1.9639; -0.8879; 0.1115]^T$	$[-1.9802; -0.9286; 0.0964]^T$
$\%\boldsymbol{\sigma}^1$	$[0.1870; 0.2517; 2.0380]^T\%$	$[0.1919; 0.2444; 2.3360]^T\%$	$[0.1951; 0.2496; 2.7714]^T\%$
$\overline{\mathbf{n}}^2$	$[1.2866; -0.9845; 0.1158]^T$	$[1.2523; -0.9878; 0.1331]^T$	$[1.2825; -0.9600; 0.1296]^T$
$\%\boldsymbol{\sigma}^2$	$[0.2152; 0.2640; 2.4378]^T\%$	$[0.1834; 0.2173; 1.7791]^T\%$	$[0.1918; 0.2271; 1.8906]^T\%$
$\overline{\mathbf{n}}^3$	$[0.3552; 2.1675; 0.0296]^T$	$[0.3889; 2.2474; -0.0173]^T$	$[0.3589; 2.3471; -0.0549]^T$
$\%\boldsymbol{\sigma}^3$	$[0.6731; 0.2327; 11.5804]^T\%$	$[0.6015; 0.2326; 20.0572]^T\%$	$[0.6468; 0.2299; 6.4307]^T\%$

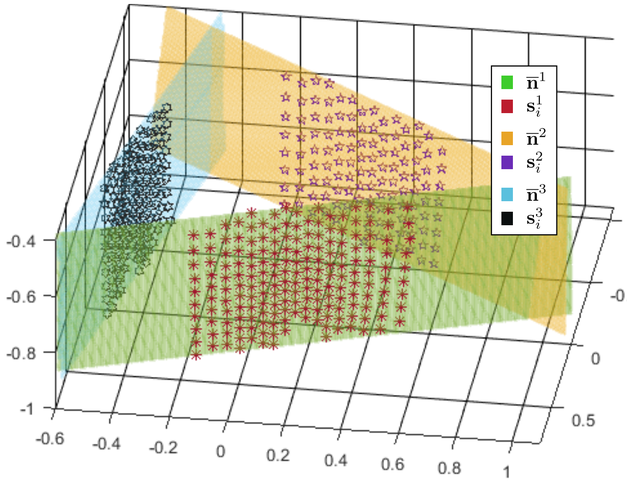

Figure 9: Data points and reconstructed surfaces

An approximation of $\mathbf{n}^j$ in the least-square sense, $\overline{\mathbf{n}^j}$, can be computed according to the solution of Eq. (16):

$$\overline{\mathbf{n}}^j = ({\mathbf{A}^j}^T \mathbf{A}^j)^{-1} {\mathbf{A}^j}^T \mathbf{1}_{\lambda_j} \tag{18}$$

and the quality of the approximated results can be evaluated by computing the 3×3 covariance matrix of $\overline{\mathbf{n}}^j$ as [26]:

$$\mathbf{C}_{\overline{\mathbf{n}}^j} = \frac{\|\mathrm{res}^j\|^2}{\lambda - 3} ({\mathbf{A}^j}^T \mathbf{A}^j)^{-1} \tag{19}$$

where:

$$\mathrm{res}^j = \mathbf{A}^j \overline{\mathbf{n}}^j - \mathbf{1}_{\lambda_j} \tag{20}$$

is the residual of model (16). Ultimately, the relative standard deviation of each component of $\overline{\mathbf{n}}^j$ is computed as:

$$\%\boldsymbol{\sigma}^j(k) = 100 \frac{\sqrt{\mathbf{C}_{\overline{\mathbf{n}}^j}(k,k)}}{|\overline{\mathbf{n}}^j(k)|}, \qquad k = 1, 2, 3 \tag{21}$$

Table II shows the results of the identified $\overline{\mathbf{n}}^j$ and the associated $\%\boldsymbol{\sigma}^j$ for 3 experiments in which the robot and the planar surfaces were left in the same configuration; prototype geometrical data are reported in Table I. A graphical representation of the reconstructed surfaces (denoted by $\overline{\mathbf{n}}^j$), compared to the data points acquired during *Test 1* (denoted as $\mathbf{s}_i^j$), is shown in Fig. 9. Figure 10 presents the typical trend of res^j for $j = 3$ in *Test 1*.

Some conclusions can be drawn from experiments:

- the values of $\overline{\mathbf{n}}^j$ in different tests are comparable, thus allowing one to infer that the repeatability of the laser scanner is acceptable (direction error between consecutive tests: max value 2.1°, mean value 1.3°);
- the laser-scanner overall accuracy can be improved; Fig. 10 shows two clearly distinct sources of error: a random noise which can be mainly attributed to the distance-measuring laser (accuracy = ±5mm@800Hz), and a curvilinear aberration of the planar surface, which can be associated with (i) oversimplified assumptions in modelling the cable robot (i.e. cable attachment points), (ii) the lack of a sophisticated calibration of the manipulator geometry due to its prototype nature.

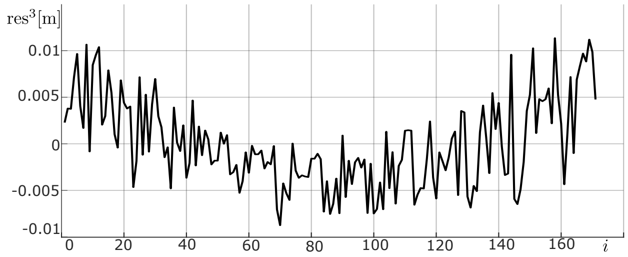

Figure 10: Residuals of *Test 1*, $j = 3$

All in all, the machine is fairly accurate in reconstructing surfaces of known shape: estimated relative standard deviations $\%\boldsymbol{\sigma}^j$ below 1% are a statistical indication that, even in presence of measurement errors, whether they originated from modelling or sensor inaccuracies, the mathematical model of the surface is correctly evaluated; in addition, an increasing value of a relative standard deviation affecting a nearly null (or limited magnitude) parameter does not affect results' accuracy.

VI. CONCLUSIONS

In this paper, a novel *CDPR* architecture with a large orientation workspace dedicated to laser-scanning operations was presented. Its orientation workspace properties were analyzed and its practical capabilities were demonstrated through prototypal design and experimental reconstruction of benchmark surfaces. Experimental results are satisfactory given the prototypal nature of the robot. The presented design shows the versatility of cable robotics and expands the range of applications in which these robotic devices may be proven to have an effective use. In the future, an advanced mechanical design of some components, as well as optimization of design parameters for a given orientation task, should be considered, in order to increase the robot accuracy.

REFERENCES

[1] H. S. Park, H. M. Lee, H. Adeli, and I. Lee, "A New Approach for Health Monitoring of Structures: Terrestrial Laser Scanning," *Computer-Aided Civil and Infrastructure Engineering*, vol. 22, no. 1, pp. 19–30, 2007.

[2] K. Kraus and N. Pfeifer, "Determination of terrain models in wooded areas with airborne laser scanner data," *ISPRS Journal of Photogrammetry and Remote Sensing*, vol. 53, no. 4, pp. 193 – 203, 1998.

[3] H. Surmann, A. Nüchter, and J. Hertzberg, "An autonomous mobile robot with a 3d laser range finder for 3d exploration and digitalization of indoor environments," *Robotics and Autonomous Systems*, vol. 45, no. 3, pp. 181 – 198, 2003.

[4] Y. Kaya, "Method and apparatus for forming the calibration chart for the underground fuel tanks," U.S. Patent 8,555,697, 2013.

[5] E. Motti, "Apparatus for the measurement of capacity of a container and associated method of measurement," EP Patent 2 650 658 B1, 2016.

[6] W. Lalo, T. Bruckmann, and D. Schramm, "Optimal Control for a Wire-Based Storage Retrieval Machine," in *New Trends in Mechanism and Machine Science*, F. Viadero and M. Ceccarelli, Eds. Dordrecht: Springer Netherlands, 2013, pp. 631–639.

[7] J. Murayama, L. Bougrila, Y. Luo, K. Akahane, S. Hasegawa, B. Hirsbrunner, and M. Sato, "SPIDAR G&G: a two-handed haptic interface for bimanual VR interaction," in *EuroHaptics*, vol. 2004, June 2004, pp. 138–146.

[8] C. Bauer, "Device and method for detecting the inventory of a selling and/or storing device, and a storage-managing system equipped with said device," WO Patent 101 248, 2012.

[9] R. Yao, X. Tang, J. Wang, and P. Huang, "Dimensional Optimization Design of the Four-Cable-Driven Parallel Manipulator in FAST," *IEEE/ASME Transactions on Mechatronics*, vol. 15, no. 6, pp. 932–941, Dec 2010.

[10] B. L. Jordan, M. A. Batalin, and W. J. Kaiser, "NIMS RD: A Rapidly Deployable Cable Based Robot," in *Proceedings 2007 IEEE International Conference on Robotics and Automation*, April 2007, pp. 144–150.

[11] S. Khalilpour, R. Khorrambakht, H. Taghirad, and P. Cardou, "Robust cascade control of a deployable cable-driven robot," *Mechanical Systems and Signal Processing*, vol. 127, pp. 513 – 530, 2019.

[12] S. Perreault, P. Cardou, C. M. Gosselin, and M. J.-D. Otis, "Geometric Determination of the Interference-Free Constant-Orientation Workspace of Parallel Cable-Driven Mechanisms," *Journal of Mechanisms and Robotics*, vol. 2, no. 3, 07 2010, 031016.

[13] M. Gouttefarde, D. Daney, and J. Merlet, "Interval-Analysis-Based Determination of the Wrench-Feasible Workspace of Parallel Cable-Driven Robots," *IEEE Transactions on Robotics*, vol. 27, no. 1, pp. 1–13, Feb 2011.

[14] S. Lessanibahri, P. Cardou, and S. Caro, "Kinetostatic Modeling of a Cable-Driven Parallel Robot Using a Tilt-Roll Wrist," in *Cable-Driven Parallel Robots*, A. Pott and T. Bruckmann, Eds. Cham: Springer International Publishing, 2019, pp. 109–120.

[15] T. Reichenbach, P. Tempel, A. Verl, and A. Pott, "Static Analysis of a Two-Platform Planar Cable-Driven Parallel Robot with Unlimited Rotation," in *Cable-Driven Parallel Robots*, A. Pott and T. Bruckmann, Eds. Cham: Springer International Publishing, 2019, pp. 121–133.

[16] M. Alemán, R. Saltaren, A. Rodriguez, G. Portilla, and J. Placencia, "Rotational workspace expansion of a planar cdpr with a circular end-effector mechanism allowing passive reconfiguration," *Robotics*, vol. 8, no. 3, 2019.

[17] M. Anson, A. Alamdari, and V. Krovi, "Orientation Workspace and Stiffness Optimization of Cable-Driven Parallel Manipulators With Base Mobility," *Journal of Mechanisms and Robotics*, vol. 9, no. 3, 03 2017, 031011.

[18] M. Vikranth Reddy, N. C. Praneet, and G. K. Ananthasuresh, "Planar Cable-Driven Robots with Enhanced Orientability," in *Cable-Driven Parallel Robots*, A. Pott and T. Bruckmann, Eds. Cham: Springer International Publishing, 2019, pp. 3–12.

[19] I. A. Bonev and J. Ryu, "A new approach to orientation workspace analysis of 6-dof parallel manipulators," *Mechanism and Machine Theory*, vol. 36, no. 1, pp. 15 – 28, 2001.

[20] J. Merlet, "Simulation of Discrete-Time Controlled Cable-Driven Parallel Robots on a Trajectory," *IEEE Transactions on Robotics*, vol. 33, no. 3, pp. 675–688, June 2017.

[21] Cong Bang Pham, Guilin Yang, and Song Huat Yeo, "Dynamic analysis of cable-driven parallel mechanisms," in *Proceedings, 2005 IEEE/ASME International Conference on Advanced Intelligent Mechatronics.*, July 2005, pp. 612–617.

[22] L. Gagliardini, S. Caro, M. Gouttefarde, P. Wenger, and A. Girin, "Optimal design of cable-driven parallel robots for large industrial structures," in *2014 IEEE International Conference on Robotics and Automation (ICRA)*, May 2014, pp. 5744–5749.

[23] J. Pusey, A. Fattah, S. Agrawal, and E. Messina, "Design and workspace analysis of a 6–6 cable-suspended parallel robot," *Mechanism and Machine Theory*, vol. 39, no. 7, pp. 761 – 778, 2004.

[24] P. Cardou, S. Bouchard, and C. Gosselin, "Kinematic-Sensitivity Indices for Dimensionally Nonhomogeneous Jacobian Matrices," *IEEE Transactions on Robotics*, vol. 26, no. 1, pp. 166–173, Feb 2010.

[25] J. P. Merlet, "Jacobian, Manipulability, Condition Number, and Accuracy of Parallel Robots," *Journal of Mechanical Design*, vol. 128, no. 1, pp. 199–206, 06 2005.

[26] T. Kariya and H. Kurata, *Generalized least squares*, J. W. . Sons, Ed. John Wiley & Sons, 2004.